Runout scaling and deposit morphology of rapid mudflows

L. Jing[1], C. Y. Kwok[1,2], Y. F. Leung[3], Z. Zhang[1,4], L. Dai[1,5]

C. Y. Kwok, fiona.kwok@hku.hk

[1]Department of Civil Engineering, The University of Hong Kong, Pokfulam Road, Hong Kong

[2]State Key Laboratory of Hydraulics and Mountain River Engineering, College of Water Resource and Hydropower, Sichuan University, Chengdu, 610065, China

[3]Department of Civil and Environmental Engineering, The Hong Kong Polytechnic University, Hung Hom, Hong Kong

[4]Department of Mathematics, Univeristy of California at San Diego, La Jolla, California 92093, USA

Abstract. Prediction of runout distance and deposit morphology is of great importance in hazard mitigation of geophysical flows, including viscoplastic mudflows. The major rheological parameters of mudflows, namely, yield stress and viscosity, are crucial factors in controlling the runout and deposition processes. However, the roles of the two parameters, especially in mudflows with high inertia, remain poorly understood, and are not accounted for in runout scaling relations with source volume. Here we investigate the effects of flow rheology on runout scaling and deposit morphology using small-scale laboratory experiments and three-dimensional numerical simulations. We find that yield stress and viscosity both influence flow velocity gained during downslope propagation of mudflows, which is strongly correlated with the runout distance; the role of yield stress is more significant than viscosity. High yield stress and low viscosity lead to an elongated deposit, where longitudinal propagation is more significant than lateral spreading. In contrast, high viscosity promotes the dominance of lateral spreading of the deposit, while low yield stress and moderate viscosity produce an initial elongate deposit, followed by a secondary surge that spreads laterally near the head of the deposit. Following appropriate scaling relations for viscosity and

---

[5] Faculty of Business and Economics, The
University of Hong Kong, Pokfulam Road,
Hong Kong

yield stress, a general scaling function is proposed to incorporate flow properties in the well-known correlation of runout distance and source volume. Our findings regarding the inertia effects and the roles of yield stress and viscosity enhance our understanding of mudflows, muddy debris flows, and other viscoplastic geophysical flows.

Keypoints:

- Experiments and simulations reveal the role of inertia and rheology (yield stress and viscosity) in the runout behavior of rapid mudflows
- Different combinations of rheological parameters are found to give rise to distinct deposit morphology
- A generalized runout scaling relation is proposed incorporating rheological parameters

1. Introduction

Geophysical flows, such as landslides, avalanches, debris flows, mudflows and lava flows, are common phenomena at the surface of the Earth. These processes of mass transport and deposition are geomorphically important and contribute to shaping the landscape [*Delannay et al.*, 2017]. Their long runout distance and large deposit area also cause substantial loss of human life, destruction of houses and facilities, and interruption of key transportation corridors. Better understanding of the depositional behavior of geophysical flows is of great value to the design of protective and mitigative measures in downslope areas [*Rickenmann*, 2005].

Despite the large variation of compositions and flow regimes, most geophysical flows can be described as a viscoplastic fluid as a first approximation [*Coussot et al.*, 1998]. They behave like a solid until submitted to a stress higher than a yield threshold; upon yielding, they start to flow like a viscous liquid [*Coussot*, 2014]. A viscoplastic fluid is commonly idealized by the Bingham model or the Herschel–Bulkley model, where a constant yield stress is used to control the transition between solid- and liquid-like behaviors [*Jeong et al.*, 2009; *Balmforth et al.*, 2014]. This idealization applies to flows of saturated plastic soil with a high content of water and fines, which are known as mudflows [*Hungr et al.*, 2014]. It is also relevant to muddy debris flows [*Takahashi*, 1981; *Kaitna et al.*, 2016], snow avalanches [*Kern et al.*, 2004; *Ancey and Bain*, 2015], lahars and lava flows [*Sakimoto and Gregg*, 2001], which exhibit a similar macroscopic behavior except for a different temperature dependency of viscosity [*Griffiths*, 2000; *Balmforth et al.*, 2014]. Submarine landslides with mainly saturated fine materials, where the ambient fluid is the same as the interstitial fluid, also fall into this category [*Zakeri et al.*, 2008, 2009]. By contrast, for coarser granular materials where the effects of particle friction and collision dominate, the Coulomb friction law [*Iverson*, 1997; *Pudasaini*, 2012] and the so-called $\mu(I)$-rheology [*Jop et al.*, 2006; *Lacaze and Kerswell*, 2009] become more relevant; they are viscoplastic models with pressure-dependent yield strength [*Forterre and Pouliquen*, 2008].

This work addresses mudflows that tend to deposit over open areas after a rapid evolution down steep inclined channels (Figure 1a), which are commonly miniaturized as an inclined flume connected to a horizontal deposition plain (Figures 1b–e). Most previous studies regarding deposition and runout focus on the well-known correlation between runout distance and source volume, or the fall height of the initial mass [*Legros*, 2002; *Issler et al.*, 2005; *Staron and Hinch*, 2007; *Staron*, 2008; *Staron and Lajeunesse*, 2009; *Roche et al.*, 2011; *Johnson et al.*, 2012; *Lucas et al.*, 2014; *Parez and Aharonov*, 2015; *de Haas et al.*, 2015]. This correlation, as merely a dimensional argument, does not consider other important parameters including the rheological properties. For Bingham fluids, it has been revealed in slumping tests over a horizontal plane that yield stress controls the runout behavior [*Staron et al.*, 2013]. At the limit of small inertia, this is expected because the yield stress represents the internal strength that counterbalances gravity [*Liu et al.*, 2016]. However, in the fast propagation and deposition of mudflows, where the inertia effect becomes relevant, the relative role of viscosity and yield stress remains unclear, especially with an inclined flow configuration. Moreover, event-specific variation of rheological characteristics may result in different deposit morphologies observed in both natural mudflows and laboratory experiments [*Balmforth et al.*, 2006; *Martinez*, 2009; *Parsons et al.*, 2001; *Hürlimann et al.*, 2015; *Ancey and Cochard*, 2009; *Cochard and Ancey*, 2009]. Some experimental deposits with a similar flume geometry are given in Figures 1b–e, where clearly different deposit shapes are observed (e.g., semi-circular, hill-shape, elongated) for a variety of materials. It is interesting to understand how material properties modify the deposit morphology. Since the flow rheology involves both yield stress and viscosity, which increase simultaneously with the particle concentration for most materials [*Kaitna et al.*, 2007; *Ancey and Cochard*, 2009], it is difficult to separate the effects of the two parameters in laboratory experiments. This suggests the need for numerical modeling, which is the major focus of this study.

In this study, we perform both numerical and physical modeling to explore the effects of rheological parameters on the runout scaling and deposit morphology of mudflows. The adopted numerical scheme solves full three-dimensional equations of viscoplastic mudflows over slopes, details of which are elaborated in Sec. 2. In Sec. 3, our experimental setup and slurry rheometry are presented. Experimental and numerical results are shown in Sec. 4, where the effects of yield stress and viscosity on the runout distance and deposit shape are studied. In Sec. 5, runout scaling with a variety of flow properties is discussed following a dimensional analysis.

2. Simulation Methodology

2.1. Modeling viscoplastic mudflows

One popular strategy of debris-flow modeling is to use the depth-averaged thin layer models [*Savage and Hutter*, 1989; *Iverson*, 1997, 2005], which have been applied to the study of the spreading and stoppage of viscoplastic flows [*Huang and Garcia*, 1997, 1998; *Balmforth et al.*, 2002, 2006; *Ancey and Cochard*, 2009]. In these models, the flows are assumed to be shallow and slow, with relatively small (i.e., order-one or lower) Reynolds number [*Balmforth et al.*, 2006]. The assumptions may be violated in certain situations, such as the initial collapse stage of the event (where material thickness may be considerable), the rapid evolution of fast-moving flows on steep slopes, and the sudden change of topology at runout. The inertia effects encountered in the fast propagation of a mudflow also pose challenges for theoretical modeling based on thin layer models. To capture these processes, which are crucial for the understanding of mudflow runout and deposition in the current work, it is necessary to consider the full solutions to the governing equations without reducing their dimensions.

Recently, numerical models that do not involve a depth-averaging process have been applied in the modeling of yield-stress flows. For instance, *Zakeri et al.* [2009] simulated submarine slurry flows with a power-law rheology using a computation fluid dynamics (CFD) solver. *Domnik and Pudasaini* [2012] proposed a non-depth-averaged flow model with the Bingham yield stress; they pointed out the importance of basal sliding by incorporating a Coulomb-like sliding law at boundaries, which is more applicable for granular flows. *von Boetticher et al.* [2016] developed a three-dimensional multiphase solver for debris flows, which treats the mixture of fines and water as a Herschel–Bulkley fluid, while the coarser granular phase is treated as a Coulomb-type flow. Similar attempts of non-depth-averaged approaches have been reported with the Coulomb-type model and $\mu(I)$-rheology [*Lagrée et al.*, 2011; *Martin et al.*, 2017; *Chauchat and Médale*, 2014]. In general, these models can reproduce all typical stages involved in a dam-break-like event, from the quick acceleration to a maximum velocity, to the deceleration toward a halt. An additional challenge posed by non-depth-averaged models is the treatment of a free fluid surface [*Scardovelli and Zaleski*, 1999]. One way to tackle this is to track the free surface using the volume of fluid (VOF) method, which defines a secondary air phase above the surface of the primary fluid phase; the values of phase fraction can be used to reconstruct the interface position. This method has been successfully used by *Zakeri et al.* [2009], *Lagrée et al.* [2011], *Staron et al.* [2013], *Liu et al.* [2016], and *Jing et al.* [2016].

In this work, we use a VOF solver `interFoam` from the open-source CFD toolbox OpenFOAM [*OpenCFD*, 2016]. The governing equations and constitutive models for a theoretical mudflow are presented with two important schemes: (i) the regularization of viscoplastic models, and (ii) the tracking of the dynamic free fluid surface.

2.2. Governing equations

The Navier-Stokes equation for conservation of momentum and mass provides the governing equations for a continuum viscoplastic flow:

$$\frac{\partial}{\partial t}\big(\rho\mathbf{u}\big) + \nabla\cdot\big(\rho\mathbf{u}\mathbf{u}\big) = -\nabla p + \nabla\cdot\mathbf{T} + \rho\mathbf{g} \tag{1a}$$

$$\nabla\cdot\mathbf{u} = 0, \tag{1b}$$

where $\mathbf{u}$ is velocity, ρ is density, p is pressure, $\mathbf{T}$ is the extra-stress tensor, and $\mathbf{g}$ is gravitational acceleration vector. The stress tensor $\mathbf{T}$ is defined by a constitutive model. A generalized constitutive description of viscoplastic fluids is the Herschel–Bulkley model, which defines $\mathbf{T}$ (or $\mathbf{D}$) as:

$$\mathbf{T} = \big(\frac{\tau_c}{\dot{\gamma}} + 2^n K\dot{\gamma}^{n-1}\big)\mathbf{D}, \tau > \tau_c \tag{2a}$$

$$\mathbf{D} = 0, \text{otherwise} \tag{2b}$$

where τ_c is the critical stress (yield stress), K is consistency, and n is a power index; $\tau = \sqrt{-T_{II}}$ is shear stress, and $T_{II} = \frac{1}{2}[(\mathrm{tr}\mathbf{T})^2 - \mathrm{tr}(\mathbf{T})^2]$ is the second invariant of the extra-stress tensor $\mathbf{T}$; shear rate $\dot{\gamma} = \sqrt{-D_{II}}$, in which $D_{II} = \frac{1}{2}[(\mathrm{tr}\mathbf{D})^2 - \mathrm{tr}(\mathbf{D})^2]$ is the second invariant of the strain rate tensor $\mathbf{D}$, and $\mathbf{D} = \frac{1}{2}(\nabla\mathbf{u} + \nabla\mathbf{u}^{\mathrm{T}})$.

A simpler model for viscoplastic fluids is the Bingham model:

$$\mathbf{T} = \left(\frac{\tau_y}{\dot{\gamma}} + \mu_B\right)\mathbf{D}, \tau > \tau_y \tag{3a}$$

$$\mathbf{D} = 0, \text{otherwise} \tag{3b}$$

where τ_y is yield stress and μ_B is Bingham viscosity. Different notation is used to distinguish from that of the Herschel–Bulkley model.

The rheological parameters (e.g., yield stress and viscosity) can be measured in a one-dimensional flow configuration, where the above three-dimensional expressions are reduced to

$$\tau = \tau_c + K\dot{\gamma}^n \tag{4}$$

for the Herschel–Bulkley model, and

$$\tau = \tau_y + \mu_B\dot{\gamma} \tag{5}$$

for the Bingham model, respectively.

2.3. Regularized viscoplasticity

The constitutive models presented above are regularized in numerical implementations to avoid the divergence of viscosity at zero rate of strain [*Frigaard and Nouar*, 2005].

For brevity, here the Bingham model for one-dimensional simple flow (equation (5)) is shown for example. The same regularization method is applied for the Herschel–Bulkley model. Several approaches for regularization have been proposed, amongst which are Tanner's bi-viscosity model [*O'Donovan and Tanner*, 1984], which is used in this work, and Papanastasiou's exponential model [*Papanastasiou and Boudouvis*, 1997]. As illustrated in Figure 2a, a critical shear rate $\dot{\gamma}_c$ is used to separate the flow curve into two segments: the first one has a high viscosity μ_0, while the second one is identical to the original Bingham model, with a viscosity μ_B. It has been found in Poiseuille flows that an optimal choice of the critical shear rate is $\dot{\gamma}_c = 0.001$ s^{-1} [*Mitsoulis*, 2007; *Jeong*, 2013]. We have tested the choice of $\dot{\gamma}_c$ and its effect becomes negligible when $\dot{\gamma}_c$ is as low as 0.001 s^{-1}. We attribute this to the fact that our study examines inertia flows having a typical shear rate of several hundred reciprocal seconds, and the low-shear rate regions contribute little to the overall flow behavior. Therefore, $\dot{\gamma}_c = 0.001$ s^{-1} is consistently adopted in the current work. However, this choice may warrant further investigation if adopted for a study focusing on a creeping regime where the shear rate is mainly small.

2.4. Free-surface tracking technique

Since the geometric configuration of a mudflow evolves continuously in the spatial and temporal dimensions, special treatments are required to track the position of its free surface: the flow is represented by a two-fluid mixture, which includes a primary fluid (here, a viscoplastic fluid) and a secondary fluid (typically, air). The bulk properties of the two-fluid mixture are weighted averages according to the volume fractions [*Berberović et al.*, 2009]. Specifically, we have bulk density $\rho = \alpha_1\rho_1 + \alpha_2\rho_2$, and bulk viscosity

$\mu = \alpha_1\mu_1 + \alpha_2\mu_2$, where α is volume fraction with subscripts 1 and 2 denoting the primary and secondary fluid phases, respectively.

The interface between the two fluids is solved using the spatial distribution of their volume fractions, which is referred to as the volume of fluid (VOF) method [*Rusche*, 2002; *Berberović et al.*, 2009]. The basic idea of the VOF method is shown in Figure 2b. Numerical cells with $\alpha_1 = 1$ represent pure fluid while $\alpha_1 = 0$ indicates air. The precise position of the interface is located by taking weighted average for the elevation of each cell. The evolution of the free surface is governed by a transport equation:

$$\frac{\partial \alpha_1}{\partial t} + \nabla \cdot \big(\alpha_1 \mathbf{u}\big) + \nabla \cdot \big(\alpha_1 (1-\alpha_1)\mathbf{u}_r\big) = 0, \tag{6}$$

where $\mathbf{u}_r$ is the liquid–air relative velocity. The third term is used to compress the interface to a sharper region [*Berberović et al.*, 2009]. The first two terms on the left-hand side have the same advection form as the continuity equation in standard mixture theory, indicating the fact that in an incompressible fluid the conservation of mass is equivalent to the conservation of volume, hence the volume fraction.

3. Small-scale Experiments and Rheometry

3.1. Experimental setup

The experimental setup consists of a Plexiglas channel with adjustable inclinations, a tank with a removable gate, and a horizontal deposition plain. Notation and local coordinates for different scenarios are shown in Figure 3. The flume is 1 m long and 0.2 m wide, the tank is 0.4 m long, and the deposition plain is a 1m × 1m square (Figure 3a). Before the start of an experiment, the channel is inclined to a designated slope angle, θ, which is in a range from 10° to 20°. The well-mixed slurry (Sec. 3.2) of volume V is gently poured into the tank and the top surface is flattened; V ranges from 2 L to 4.5 L.

During an experiment, the gate is removed rapidly to release the fluid in a dam-break fashion. The flow traveling down the slope is recorded by a video camera (Sony HDR-XR100E) until eventual deposition is achieved (Figure 3b). The video is postprocessed with an OpticalFlow program (Matlab Computer Vision System Toolbox$^{\mathrm{TM}}$), which analyzes the velocity distributions of objects in each image. It can sharply delineate the free surface of the mudflow. Typical results from the postprocessing include evolution of flow-depth profile, front position and frontal velocity of the mudflow; an example is given in Sec. 4.2. After the flow becomes stationary, deposit runout length (L_r) and maximum width (W_m) are measured (Figure 3c). Note that L_r is the distance from the toe of the slope. On the deposition plain, deposit-depth contours are measured at a set of 5 cm-by-5 cm grid points using a ruler with a precision of 1 mm. Repeatability has been verified by conducting identical flume tests under the same temperature and humidity conditions (see Figure S1 in the supporting information).

3.2. Slurry rheometry

The slurry used is water–kaolin mixtures at different volume concentrations (C_v). The slurry rheology is measured on a Brookfield rheometer (R/S SST200), which has a coaxial cylinder measurement geometry. The fluid container has vertical ribs to avoid slippage during the measurement. Typically, 10 specimens are prepared from the same mixture to determine a master flow curve. Figure 4a shows the flow curves for five concentrations with error bars representing the standard deviation of measurements. The error bars are generally smaller than the symbols.

Two rheological models for a simple shear flow (i.e., the Herschel–Bulkley model (equation (4)) and Bingham model (equation (5))) are adopted to fit the rheometrical data. As seen in Figure 4a, the Herschel–Bulkley model closely describes the flow behavior in the full range of shear rate, while the Bingham fitting is obtained for a specific range ($200 - 800$ s^{-1}), according to the typical values of shear rate estimated by considering the typical flow velocity and flow thickness in our flume tests. Although this range may not apply to all locations within the flow, it does represent the majority of the flow. The obtained "yield stress" is then the intersection of the fitted line with the vertical axis, which represents a phenomenological parameter rather than the real yield stress of the material; to find the real yield stress is a more complicated task that lies beyond the scope of this work [*Balmforth et al.*, 2014]. In fact, we stress that all rheological parameters in the Bingham and Herschel–Bulkely models are fitting parameters of the flow curves, rather than actual material properties. Note also that in a Bingham fitting the omitted data at lower shear rates does not affect the results significantly because the stoppage phase is very rapid in our inertia flows. It is confirmed in Sec. 4.2 that using the Bingham model yields nearly identical results with the Herschel–Bulkley model in the current flow configuration.

Table 1 lists the fitting parameters for all measured concentrations, based on equation (4) and equation (5); the parameters are adopted as direct input for our numerical modeling. Since our major interest is to understand the effects of yield stress and viscosity, for simplicity, we mainly adopt the Bingham model in the subsequent analysis. Note that yield stress (τ_y) and viscosity (μ_B) in the rest of this paper refer to the parameters determined by Bingham fittings. In Figures 4b and c, τ_y and μ_B are plotted against C_v, respectively. It can be seen that both yield stress and viscosity increase exponentially with volume concentration.

4. Experimental and Numerical Results

4.1. Summarized results of different experimental series

Table 2 summarizes the observed deposit geometry (runout length and maximum width) for different imposed volume concentrations, slope angles and mudflow volumes. The series of reference cases contains four major experiments with varying concentrations ($C_v = 18\%, 19\%, 20\%, 21.1\%$) and a fixed combination of volume and slope angle ($V = 3$ L and $\theta = 14°$). One of the reference cases is used to demonstrate the typical experimental results and the validation of numerical models in Sec. 4.2, following which the effects of varying concentration are discussed in Sec. 4.3. Then, the roles of viscosity and yield stress are studied in detail with numerical simulations in Sec. 4.4. In other series, volume and slope angle are varied for different concentrations, respectively. The effects of these variations on runout distance are discussed in Sec. 4.5.

4.2. Typical experimental results and model validation

The experiment with $V = 3$ L, $\theta = 14°$, $C_v = 20\%$ is employed to illustrate typical experimental results and to validate our numerical models. The accuracy of other numerical simulations is similar across all experimental cases (a comparison of the predicted and experimental deposit morphology for different volume concentrations can be found later in Figure 9). In numerical simulations, the input rheological parameters for both Bingham and Herschel–Bulkley models follow those listed in Table 1, and no calibration or inverse analysis for these parameters is needed. A no-slip boundary condition is imposed in the numerical simulations, which matches our observations of no slip during the flume tests. We have verified this by covering the Plexiglas with sandpaper, which has a negligible influence on the results (see Figure S2 in the supporting information). The minimum time step used in the simulations is 10^{-3} s, which ensures numerical stability. The mesh size used in the simulations is generally 5 mm; the computation converges at this resolution. A numerical simulation is considered complete when the outer edge of a deposit does not expand with time, and then the final runout distance and deposit morphology are obtained. Turbulence is not considered due to the viscous effect of mudflows. Indeed, all flume tests exhibit a laminar behavior according to our observations. A more quantitative discussion of the laminar behavior can be found in Sec. 5.2. A sample script of this validation case is provided in the supporting information.

Figure 5 validates the simulations with the flow-depth profiles detected using OpticalFlow. Note that in Figures 5, the line segments without markers represent conditions where no motion is detected at a specific moment. For these segments, the past free surface is patched to the present profile, due to the fact that slurry tends to attach to the sidewalls. The affected area is mostly close to the region of initial release, while our primary concern is the flow front. As seen in Figures 5d–f, the agreement between experimental and numerical results is generally good. Note that the sharp peaks behind the front in numerical simulations result from the shape of the initial mass, while such structures are smeared in the experimental images due to gate removal and the attachment of slurry on the sidewall.

In Figures 6a and b, the measured front position (x_f) and front velocity (u_f) of the mudflow along the channel are plotted as a function of travel time (t) and x_f, respectively, and the numerical predictions are shown to agree with the experimental results. It takes less than 1 s for the slurry to reach the toe of the slope, and three stages can be identified, namely, a sudden acceleration to the peak velocity ($u_{\max}$), a plateau where velocity varies less significantly, and a tendency to decelerate toward stoppage. Deceleration occurs as the slurry stretches; the shear forces provided by walls, as well as the yield strength of slurry, tend to balance the driving forces provided by gravity. The front velocity remains high ($\sim$ 1 m/s) right before runout occurs (Figure 6b). The velocity at runout, however, can be rapidly dissipated as the flow spreads and deposits over the deposition plain.

On the deposition plain, numerical simulations produce good results of the final deposit; both the outer-most profile (Figure 6c) and deposit depth (Figures 6d and e) agree well with the experimental measurements. Key features of the slurry deposit are captured: (i) the deposit shape is elongated, due to the rapid arrest, with a slightly wider lobe behind the tip; (ii) the lobe area has a flat surface off the edge (the contour of 11 mm); (iii) steep depth gradients are found near the edge.

4.3. Effects of volume concentration

The results of the four reference cases are presented to study the effects of concentration on front propagation and final deposition, with C_v varying from 18% to 21.1%. As C_v increases, yield stress and viscosity increase simultaneously (Table 1 and Figure 4).

Figure 7 shows the flow kinetics on the channel. It can be seen that when $t < 0.2$ s, the evolution of the front position is independent of flow properties (Figure 7a). This corresponds to the first stage ($x_f < 0.18$ m) identified in Figure 7b, where u_f rises above 1 m/s in the first 0.18 m traveled. These results indicate that at the initial collapse triggered by gravity, the frontal motion does not depend on rheological properties. After the initial stage, a higher concentration tends to hinder the propagation of the frontal wave (Figure 7a). The second stage in Figure 7b, where the velocity evolves steadily, is shortened as the concentration increases. At the same time, higher concentrations lower the peak velocity that marks the mobility gained through acceleration, leading to a longer flow duration. As the flow stretches to a certain length, the driving component of gravity down slope cannot overcome the internal flow strength and the drag provided by walls. This length, at which the flow starts to decelerate, decreases with the increasing concentration (Figure 7b). Indeed, a more concentrated slurry tends to counterbalance gravity more efficiently. Note that the result for the 20% case deviates slightly from the overall trend, which stems from the fluctuation of material properties observed in Figure 4c (i.e., the measured μ_B for the 20% slurry is close to the 19% slurry).

Figure 8 shows the final deposits of the four experiments. The profile of an experimental deposit is less elongated as C_v increases (Figure 8a). However, the maximum deposit width remains similar. When $C_v = 21.1\%$, the runout distance is the shortest, and the maximum lateral spreading occurs near the outlet of the channel. When $C_v = 18\%$, the deposit exhibits a waist-like region around $x = 0.2$ m, beyond which the width increases slightly and the maximum is reached at around $x = 0.62$ m. Figure 8b presents the depth profiles at the centerline of the deposition plain ($z = 0$). As the deposit is elongated at lower concentrations, its depth is lower. The top surface at the center section for all cases is generally flat. Slurries are accumulated at the toe of the slope ($x = 0$). Near the front edge, the flow depth drops rapidly to zero.

The understanding of deposit morphology can be further enhanced by numerical simulations. Photos of the final deposits taken after the experiments (overlaid by measured depth contours), together with the contour plots and three-dimensional mesh plots obtained from numerical simulations, are shown in Figure 9. It can be seen that good agreement is achieved for all cases, as pointed out in Sec. 4.2, without any calibration of simulation parameters. The numerical results show that the deposit lobe is generally flat and wide followed by an elongated 'waist' near the outlet of the flume (which becomes less obvious when $C_v = 21.1\%$). Since the slurries come to a halt very rapidly (within 2 s), the lateral spreading right after runout is not significant, while the deposition takes place mainly along the streamwise direction. The steep edge is a key feature of viscoplastic fluids, which is attributed to the effect of yield stress [*Coussot*, 1997]. Indeed, as concentration increases, yield stress increases and the depth gradient is steeper at the front edge. In fact, at higher concentrations, more of the slurry remains on the channel and the volume of the deposit on the deposition plain is small. Therefore, the yield stress plays an essential role in the depositional behavior of slurries. Meanwhile, the increase of viscosity also reduces flow mobility and thus hinders runout. The roles of viscosity and yield stress are elaborated in the next section.

4.4. Roles of viscosity and yield stress

It should be noted that if a slurry is released gently (e.g., on a horizontal plane), the final deposit shape is known *a priori* from theory and essentially depends on the yield stress of the material; the viscosity should not play a role during the creeping stoppage of the flow [*Coussot and Proust*, 1996; *Balmforth et al.*, 2006; *Liu et al.*, 2016]. However, a major difference in our current inclined configuration is that the flow gains a high kinetic energy on the steep channel and stops rapidly after its runout on the deposition plain. In this case, the flow inertia has a major impact on the flow characteristics and deposition behaviors. The inertia effect is expected to depend on both yield stress and viscosity.

Since viscosity and yield stress increase simultaneously with volume concentration (Figure 4), it is difficult to isolate the effects of the two rheological parameters. In numerical simulations, this can be achieved by examining different combinations of τ_y and μ_B within the range observed in prior studies (Figure 10). The parameter space of our simulations is shown as the rectangular zone in Figure 10, where τ_y varies from 10 Pa to 50 Pa, and μ_B ranges between 0.01 $\mathrm{Pa \cdot s}$ and 1 $\mathrm{Pa \cdot s}$. The lowest value of μ_B is chosen to be close to our 18% slurry; in our experiments the 17% mudflow runs out of the depositional plain. The parameter space is considered to be realistic because it encompasses the characteristics of several kinds of slurries, including the one used in our experiments (Table 1) and those reported in the literature [*Coussot*, 1997; *Martinez*, 2009; *Kaitna et al.*, 2007]. Note that the initial volume ($V = 3$ L) and slope angle ($\theta = 14^\circ$) remain unaltered in these cases.

Figures 11a and b show the effects of these two parameters (i.e., yield stress and viscosity) on the runout distance. In general, the increase of both parameters tends to hinder the runout distance, and the trends are similar for any given value of μ_B or τ_y. Intuitively, viscosity controls the time scale of front propagation, while yield stress takes effect mainly where shear rate is low (e.g., near the free surface). However, the results show that both parameters contribute similarly to the final runout distance. A similar effect can be found on the flow mobility (i.e., the peak frontal velocity $u_{\max}$ on the channel) that both yield stress and viscosity reduce the mobility of a mudflow (Figures 11c and d). This may explain the aforementioned effect of the two parameters on L_r, since the mobility of a flow has a first-order impact on the maximum distance it can reach after runout. Indeed, a strong correlation is found between $u_{\max}$ and L_r in Figure 11e, indicating that in the current configuration viscosity or yield stress affects the runout by modifying the flow mobility, which is clearly an inertia effect.

Since the plots in Figures 11a and b show a similarity in shape, one can collapse the data into a single empirical relation, such that L_r is correlated with $\tau_y \mu_B^{0.35}$ (Figure 11f). It indicates that although both μ_B and τ_y contribute to the runout distance of mudflows, the role played by τ_y is more significant. The relation between $u_{\max}$ and $\tau_y \mu_B$ is similar to Figure 11f (not shown for brevity), since $u_{\max}$ is linearly related to L_r (Figure 11e). Such a conclusion is consistent with the results of slumping tests on a horizontal plane, which revealed that yield stress has a more profound influence on runout distance [*Staron et al.*, 2013].

On the other hand, Figure 12 shows how yield stress and viscosity are predicted to control the deposit morphology of viscoplastic fluids. In general, low viscosity ($\mu_B = 0.01 \sim 0.1$ Pa $\cdot$ s) and high yield stress ($20 \sim 30$ Pa) can produce deposits that are similar to our laboratory slurries and those in Figures 1d and e, which tend to be elongated with little lateral spreading. In these cases, the deposition process is fast (μ_B is low), so that no subsequent surges smear the initial deposit. The initial shape can be retained owing to the high internal strength (high τ_y), and a part of the flow remains stuck on the slope and sidewalls. The hill-shape deposit (similar to Figure 1c) observed in the top-middle zone of Figure 12 is a result of the slow motion of secondary surges. While the first surge can reach a longer runout distance, the rest of the flow reaches the outlet and starts to spread laterally with very low velocity (since μ_B is high). When μ_B further increases (i.e., at the top-right corner of Figure 12), the lateral spreading dominates over the longitudinal runout, which leads to a semi-circular deposit shape similar to Figure 1b. When both μ_B and τ_y are high (the bottom-right corner), the entire flow is slow. Deposition occurs during the course of flow, such that not much of the flow runs out of the channel onto the deposition plain. When the two rheological parameters are small (toward the top-left corner), the flow tends to rapidly spread across the deposition plain (becoming similar to water).

4.5. Effects of volume and slope angle

In the previous discussion, volume V and slope angle θ are not varied, since the focus is on how rheological parameters influence the depositional behavior. As two major geometric factors, the effects of V and θ are relatively straightforward for mudflows, unless a change of flow regime emerges (e.g., roll-wave instability may be observed when $V > 4L$ and $\theta > 15°$; not discussed in this research). In Figure 13, both experimental and numerical results with varying V and θ are presented. The scenarios for these experiments can be found in Table 2. In general, L_r increases linearly when V increases from 2 L to 4 L with $\theta = 14°$, and when θ increases from 12° to 16° with $V = 3$ L.

In the literature, different mechanisms have been proposed to explain the increase of L_r with V, such as the sliding and spreading mechanism by *Staron and Lajeunesse* [2009] and the frictional velocity-weakening mechanism by *Lucas et al.* [2014]. The frictional velocity weakening is more relevant to granular avalanches. In our mudflows, the linear correlation between L_r and V is mainly due to a geometric effect. Since the slurries tend to spread over a constant base area of the channel, the runout length should grow at first order as $V^{1/3}$, thus the linear correlation. This geometric effect is similar to the spreading mechanism proposed by *Staron and Lajeunesse* [2009].

5. Scaling from Lab-scale to Field-scale

Experimental results from small scales can have direct geotechnical and geological relevance to field responses only if appropriate scaling is considered. *Iverson* [2015] pointed out in a dimensional analysis that miniaturized debris flows exhibit disproportionately large effects of viscous shear resistance and small effects of excess pore-fluid pressure. This warrants the necessity of conducting debris flow experiments at the largest possible scale. Nevertheless, since mudflows are considered as homogeneous and the interstitial effect is negligible in the current context, a perfect scaling may be established mathematically for this particular flow type. In the following, we first establish a correlation between runout distance and source volume using selected data from the literature, together with our experimental and numerical results. Then, scaling laws for mudflows are derived and verified with numerical simulations. Finally, the runout scaling relation with source volume is refined by incorporating the two rheological parameters (i.e., yield stress and viscosity) into a general scaling function.

5.1. Correlation between runout distance and source volume

The data we collect from the literature involve mainly slurries or Bingham-type natural debris flows, which include small-scale experiments with kaolin–water slurries [*Martinez*, 2009], laboratory flume tests with debris flow materials from the Tsing Shan landslide, Hong Kong [*Chan*, 2001], in-situ data of the Tsing Shan landslide [*Sham*, 2015], and natural volcanic landslides [*Legros*, 2002]. In all these studies, the Bingham model was reported to be used for fitting flow properties, which indicates that these flows exhibit a similar viscoplastic behavior as the slurry flows in the present study. Together with our experimental results, all data points exhibit an excellent linear correlation between $\hat{L}_r$

and V (Figure 14a). Note that the overall horizontal distance ($\hat{L_r}$, defined in Figure 3c) is used to account for the fact that the slope angle and channel length may vary in different flume systems and natural hillsides. Note also that in this section we use cubic meters as the unit of volume for generality, in contrast to the conventional unit of liters used in the previous sections when experimental data are described. The squares in Figure 14a are numerical simulations to be discussed later.

5.2. Verification of mudflow scaling

Although the linear correlation between L_r and V has been extensively reported, and V seems to be a sole first-order factor of the runout distance, the runout behavior is expected to depend also on flow properties [*Legros*, 2002; *Issler et al.*, 2005; *Staron and Hinch*, 2007; *Staron*, 2008; *Staron and Lajeunesse*, 2009; *Roche et al.*, 2011; *Johnson et al.*, 2012; *Lucas et al.*, 2014; *Parez and Aharonov*, 2015; *de Haas et al.*, 2015]. On one hand, the relevant parameters differ among different types of debris flows, a good example being the dry rock avalanche whose overall flow mobility (or, effective coefficient of friction) is a function of inter-grain friction [*Staron and Hinch*, 2007]. On the other hand, across a wide range of length scales, flow properties (e.g., yield stress and viscosity) need to be appropriately scaled to accurately describe the behavior of natural debris flows. For instance, the energy expenditure necessary to overcome a yield strength at a small thickness (e.g., 0.01 m in our flume system) may be largely irrelevant at the real scale of 1 ∼ 10 m thickness [*Iverson*, 2015].

To understand how the properties of a viscoplastic debris flow can be appropriately scaled, a dimensional analysis is performed (Appendix A), showing that a proper scaling with the length scale H can be achieved with the following rules being respected:

$$\frac{\mu_{B1}}{\mu_{B2}} = \left(\frac{H_1}{H_2}\right)^{\frac{3}{2}},\ \frac{\tau_{y1}}{\tau_{y2}} = \frac{H_1}{H_2}, \tag{7}$$

where subscripts 1 and 2 represent two arbitrary length scales. These rules are to be verified with numerical simulations at different scales.

Let the initial flow depth at the gate, h_g, be the characteristic height at our laboratory scale, where scale number $N = 1$. In numerical simulations, the flume is scaled up to $N = 10, 100, 1000, 10000, 100000$, so that the characteristic height becomes Nh_g, and the source volume is scaled by N^3. To maintain dynamic similitude, yield stress and viscosity are scaled by $N^{3/2}$ and N, respectively, according to equation (7). The dimensionless viscosity, $M = \mu_B/\rho\sqrt{gh_g^3}$, and dimensionless yield stress, $T = \tau_y/\rho g h_g$, can be calculated as $M = 0.00014, 0.00018, 0.00020, 0.00028$ and $T = 0.061, 0.078, 0.099, 0.13$, respectively. Good dynamic similarities are achieved in the numerical simulations across different scales. As shown in Figure 15, both the runout distance, L_r, and the maximum width of the deposits, W_m, are well scaled by N.

This scaling test shows that our dimensionless flow properties control the dynamic similarity of mudflows. Alternatively, they can be interpreted in terms of the Reynolds number (Re) and Bingham number (Bi) as presented in Appendix A. In fact, if $\sqrt{gh_g}$ is chosen as the characteristic flow velocity in our inertia flows, we have

$$\mathrm{Re} = \frac{\rho}{\mu_B}\sqrt{gh_g^3},\ \mathrm{Bi} = \frac{\tau_y}{\mu_B}\sqrt{\frac{h_g}{g}}, \tag{8}$$

leading to $\mathrm{Re} = 1/M$ and $\mathrm{Bi} = T/M$. Therefore, we can estimate the ranges of characteristic Re and Bi as $3000 \sim 7000$ and $400 \sim 500$, respectively. The high value of Re reflects the rapid propagation and high inertia of our mudflows. Note that the range of

Re (thus the flow regime) matches with those reported in previous experiments, such as the $2.3 \times 10^4 \sim 1.4 \times 10^5$ for small-scale flume tests [*de Haas et al.*, 2015] and 3×10^3 for large-scale USGS flume tests [*Iverson et al.*, 2010]. Meanwhile, turbulence is not relevant in our cases because of the high Bingham number [*Malin*, 1997]. According to *Malin* [1997], when the Hedstrom number ($\mathrm{He} = \mathrm{Re} \cdot \mathrm{Bi}$) has an order of magnitude value of 10^6, the critical Re for laminar-turbulent transition is beyond 10^4.

5.3. A general scaling function

Numerical simulations at various scales allow the refinement of the correlation found in Figure 14a. In Figure 14b, we correlate L_r with $V^{1/3}$ to propose a general scaling function. Note that $V^{1/3}$ is used such that the prefactor and exponent of the power-law function are dimensionless (see equation (9)).

Different straight lines are fitted for the four combinations of M and T, which are almost parallel with a slope of 1.00 ± 0.01 (Figure 14b). To show how the lines are affected by M and T, we define L_r^1 as the runout distance (from the toe of the slope) corresponding to $V^{1/3} = 1$ m, thus $L_r^1 = 6.446, 4.752, 3.231, 1.708$ m for increasing M and T. Noting that for a given geometry, μ_B and τ_y are roughly correlated for commonly encountered slurries (Figure 10), T is employed as the only factor of L_r^1 to reduce the complexity of this analysis. As shown in the inset of Figure 14b, L_r^1 decreases linearly with T (i.e., $L_r^1 = \mathcal{L}(T) = 10.48 - 70.79T$), so that we can write L_r as a function of T and V (i.e., $L_r = \mathcal{L}(T)V^{1/3}$).

In a more general sense, let P represent the properties of a geophysical flow, which can be the yield stress and viscosity of a mudflow, or the internal friction angle of a granular avalanche. One can write

$$L_r = \mathcal{F}_1(P)\Big(V^{\frac{1}{3}}\Big)^{\mathcal{F}_2(P)}, \tag{9}$$

where $\mathcal{F}_1$ and $\mathcal{F}_2$ are unknown functions of P. In this work (Figure 14b), we have $\mathcal{F}_1 = L_r^1 = 10.48 - 70.79T$ and $\mathcal{F}_2 = 1$. In *Staron et al.* [2013], a similar analysis on the slumping of Bingham fluids found that $\mathcal{F}_1 = \mathcal{F}_1(T, M^{-0.2})$ and $\mathcal{F}_2 = \mathcal{F}_2(T^{-1}, M^{-1})$, which also reveals that T has a more profound effect on the runout behavior than M. For other types of landslides, *Staron and Hinch* [2007] found $\mathcal{F}_1 = \mathcal{F}_1(\mu_p)$ for rock avalanches using discrete element modeling, where μ_p is the inter-particle coefficient of friction.

For debris flows involving both a muddy fluid phase and a particulate phase (i.e., grains), a scaling law similar to equation (9) is expected but the two functions, $\mathcal{F}_1$ and $\mathcal{F}_2$, may be more complicated with more unknown physical properties. Scaling of such complicated flows based on small-scale experiments is non-trivial, due to the disproportionately small effects of excess pore-fluid pressure noted by *Iverson* [2015]. Alternatively, full-scale numerical simulations, as employed in this work, may be a productive means for exploring the deposition and runout behaviors of these complicated debris flows. The numerical modeling of pure viscoplastic muddy flows presented here is a first step toward this goal. It provides a basis for the multi-phase modeling of debris flows, where the fluid phase is modeled by simulation techniques, such as computational fluid dynamics (CFD) and the lattice-Boltzmann method (LBM), while the granular phase is captured by the discrete element method (DEM). Recent progress has been made in applying the LBM-DEM system for modeling debris flows, where the muddy fluid phase is modeled by a Bingham fluid [*Leonardi et al.*, 2015, 2016]. A CFD–DEM framework for the modeling of debris flows has been discussed in *Jing et al.* [2016], to which the knowledge gained in the current study using CFD can be readily applied.

6. Conclusions

In this study, small-scale laboratory flume experiments and three-dimensional simulations are carried out to study the depositional mechanism of clay–water mixtures, which is relevant to mudflows or other muddy-type geophysical flows in nature. The effects of rheological parameters, slope angle, and volume are investigated, with a major focus on the different roles played by the two main rheological parameters, namely, viscosity and yield stress. It has been found that the increase of both parameters tends to hinder the runout distance, while the yield stress dominates the processes of runout and deposition. The deposition of slurry-like materials is rapid due to its relatively low viscosity, thus exhibiting an elongated shape, where longitudinal spreading is more significant than its lateral counterpart. The deposit typically exhibits sharp edges, and a substantial amount of material remains in the source channel due to the effect of high yield stress. Different combinations of yield stress and viscosity give rise to different deposit morphology, such as hill-like and semi-circular shapes.

To upscale the laboratory findings, numerical simulations are first validated against flume tests, and then carried out across a wide range of length scales. A linear correlation is found between runout distance and source volume, using data collected from documented laboratory experiments and field investigations. To achieve relevant results at different length scales in numerical simulations, a dimensional analysis is performed to establish appropriate scaling relations for viscosity and yield stress. The relations are verified by numerical results that exhibit an excellent similarity from lab-scale to field-scale. Based on the simulations, a general scaling function is proposed to incorporate flow properties in the well-known correlation of runout distance and source volume. Although the specific numbers reported in our general law depends on the specific configuration of our experiments, the basic form that correlates runout and volume, with flow properties considered, should apply to other debris flow-related problems in future investigations.

Appendix A: Dimensional analysis of viscoplastic debris flow

Here we first present a dimensional analysis following the Buckingham π-theorem, which yields the dimensionless form of yield stress and viscosity in a viscoplastic flow, and then show alternatively the dimensionless governing equations where these dimensionless parameters appear.

For a viscoplastic mudflow, basic physical properties include its density ρ, viscosity μ, and yield strength τ_y. Fluid compressibility is neglected. Pore pressure, permeability, gain properties, and stress induced by the particulate phase are considered as irrelevant since pore-scale mechanisms do not dominate in the propagation of mudflows. However, we note that pore pressure can be a key factor in other debris flows with notable particle interactions [*Iverson*, 2015]. Together with length L, height H, gravitational acceleration g, slope angle θ, time t, and fluid stress σ, one can write the average velocity u as a function of these listed variables,

$$u = f_1(g, L, H, t, \theta, \rho, \sigma, \mu, \tau_y), \tag{A1}$$

where f_1 is an unknown function. Excluding the dimensionless variable θ, a generic form can be postulated as

$$u = \kappa g^a L^b H^c \rho^d \sigma^e \mu^f \tau_y^g, \tag{A2}$$

where superscripts a, b, c, d, e, f and g are unknown and κ is a dimensionless proportionality factor. Recasting the dimensions of all above variables into combinations of mass $[M]$, length $[L]$, and time $[T]$, we have

$$\frac{[L]}{[T]} = \Big(\frac{[L]}{[T]^2}\Big)^a [L]^b [L]^c [T]^d \Big(\frac{[M]}{[L]^3}\Big)^e \Big(\frac{[M]}{[L][T]^2}\Big)^f \Big(\frac{[M]}{[L][T]}\Big)^g \Big(\frac{[M]}{[L][T]^2}\Big)^h \tag{A3}$$

Eliminating a, b, e based on the dimensional harmony of $[M]$, $[L]$ and $[T]$, we regroup equation (A2) as

$$u = \sqrt{gL}\Big(\frac{h}{L}\Big)^c \Big(\frac{t}{\sqrt{L/g}}\Big)^d \Big(\frac{\sigma}{\rho g L}\Big)^f \Big(\frac{\mu}{\rho\sqrt{gL^3}}\Big)^g \Big(\frac{\tau_y}{\rho g L}\Big)^h \tag{A4}$$

Note that in gravity-driven mudflows, it is appropriate to scale stress-related terms by H rather than L. Dividing equation (A4) by $\sqrt{gL}$ and reintroducing θ, we have

$$\frac{u}{\sqrt{gL}} = f_2\Big(\frac{h}{L}, \frac{t}{\sqrt{L/g}}, \frac{\sigma}{\rho g H}, \frac{\mu}{\rho\sqrt{gH^3}}, \frac{\tau_y}{\rho g H}, \theta\Big), \tag{A5}$$

where f_2 is an unknown function for the dimensionless variables. The scaling relations for the two key fluid properties are defined as

$$M = \frac{\mu}{\rho\sqrt{gH^3}},\ T = \frac{\tau_y}{\rho g H}, \tag{A6}$$

where M and T are dimensionless viscosity and yield stress, respectively. If we omit the variation of fluid density at different scales and consider g as constant, the scaling of viscosity and yield stress can be simplified to

$$\frac{\mu_1}{\mu_2} = \Big(\frac{H_1}{H_2}\Big)^{\frac{3}{2}},\ \frac{\tau_{y1}}{\tau_{y2}} = \frac{H_1}{H_2}, \tag{A7}$$

where subscripts 1 and 2 represent two arbitrary length scales.

Alternatively, the dimensionless governing equations for a Bingham fluid flow can be derived from

$$\frac{\partial}{\partial t}(\rho \mathbf{u}) + \nabla \cdot (\rho \mathbf{u}\mathbf{u}) = -\nabla p + \nabla \cdot (\frac{\tau_y}{\dot{\gamma}} + \mu)\mathbf{D} + \rho \mathbf{g} \tag{A8a}$$

$$\nabla \cdot \mathbf{u} = 0, \tag{A8b}$$

with $\mathbf{D} = 0$ if $\tau < \tau_y$, to

$$\frac{\partial \mathbf{u}^*}{\partial t^*} + \nabla^* \cdot (\mathbf{u}^* \mathbf{u}^*) = -\nabla^* p^* + \nabla^* \cdot (\frac{\tau_y}{\rho g H}\frac{1}{\dot{\gamma}^*} + \frac{\mu}{\rho H \sqrt{gH}})\mathbf{D}^* + \mathbf{g}/g \tag{A9a}$$

$$\nabla^* \cdot \mathbf{u}^* = 0, \tag{A9b}$$

with $\mathbf{D}^* = 0$ if $\tau^* < \tau_y/\rho g H$, by applying the following scalings:

$$\mathbf{u}^* = \frac{\mathbf{u}}{\sqrt{gH}}, t^* = \frac{t}{\sqrt{H/g}}, p^* = \frac{p}{\rho g H}, \mathbf{D}^* = \frac{\mathbf{D}}{\sqrt{g/H}}, \dot{\gamma}^* = \frac{\dot{\gamma}}{\sqrt{g/H}}, \tau^* = \frac{\tau}{\rho g H}, \nabla^* = \frac{\nabla}{1/H} \tag{A10}$$

Note that in the stress term, $\tau_y/\rho g H$ and $\mu/\rho H\sqrt{gH}$ are exactly the dimensionless parameters, T and M, obtained from the previous dimensional analysis. In fact, such a consistency is due to the choices of velocity scale $\sqrt{gH}$ and length scale H. Note also that the Bingham number, Bi, does not appear in the current dimensionless governing equations, which is in contrast to the case for creeping flows where a different velocity scale, $\rho g H^2/\mu$, is generally used (e.g., *Liu et al.* [2016]). Nevertheless, applying the velocity scale $U = \sqrt{gH}$ we have

$$\mathrm{Re} = \frac{\rho H U}{\mu} = \frac{\rho}{\mu}\sqrt{gH^3},\ \mathrm{Bi} = \frac{\tau_y H}{\mu U} = \frac{\tau_y}{\mu}\sqrt{\frac{H}{g}}, \tag{A11}$$

leading to $\mathrm{Re} = 1/M$ and $\mathrm{Bi} = T/M$, respectively.

Acknowledgments. The work was supported by Research Grants Council of Hong Kong (Grant No. 17203614), the open funding (No. SKHL1610) of the State Key Laboratory of Hydraulics and Mountain River Engineering (Sichuan University), and the Research Institute for Sustainable Urban Development at The Hong Kong Polytechnic University. This research was conducted in part using the research computing facilities and advisory services offered by Information Technology Services, the University of Hong Kong. Data that can be used to reproduce major figures of this paper are available as supplementary data sets. The authors are grateful for the constructive comments from three anonymous reviewers and the Associate Editor.

References

Ancey, C., and V. Bain (2015), Dynamics of glide avalanches and snow gliding, *Reviews of Geophysics*, *53*(3), 2015RG000491, doi:10.1002/2015RG000491.

Ancey, C., and S. Cochard (2009), The dam-break problem for Herschel–Bulkley viscoplastic fluids down steep flumes, *Journal of Non-Newtonian Fluid Mechanics*, *158*(1–3), 18–35, doi:10.1016/j.jnnfm.2008.08.008.

Balmforth, N. J., R. V. Craster, and R. Sassi (2002), Shallow viscoplastic flow on an inclined plane, *Journal of Fluid Mechanics*, *470*, 1–29, doi:10.1017/S0022112002001660.

Balmforth, N. J., R. V. Craster, A. C. Rust, and R. Sassi (2006), Viscoplastic flow over an inclined surface, *Journal of Non-Newtonian Fluid Mechanics*, *139*(1-2), 103–127, doi:10.1016/j.jnnfm.2006.07.010.

Balmforth, N. J., I. A. Frigaard, and G. Ovarlez (2014), Yielding to Stress: Recent Developments in Viscoplastic Fluid Mechanics, *Annual Review of Fluid Mechanics*, *46*(1), 121–146, doi:10.1146/annurev-fluid-010313-141424.

Berberović, E., N. P. van Hinsberg, S. Jakirlić, I. V. Roisman, and C. Tropea (2009), Drop impact onto a liquid layer of finite thickness: Dynamics of the cavity evolution, *Physical Review E*, *79*(3), 036306, doi:10.1103/PhysRevE.79.036306.

Chan, C. P. L. (2001), Runout distance of debris flows : experimental and numerical simulations, Thesis, The Hong Kong Polytechnic University.

Chauchat, J., and M. Médale (2014), A three-dimensional numerical model for dense granular flows based on the μ(I) rheology, *Journal of Computational Physics*, *256*, 696–712, doi:10.1016/j.jcp.2013.09.004.

Cochard, S., and C. Ancey (2009), Experimental investigation of the spreading of viscoplastic fluids on inclined planes, *Journal of Non-Newtonian Fluid Mechanics*, *158*(1–3), 73–84, doi:10.1016/j.jnnfm.2008.08.007.

Coussot, P. (1997), *Mudflow Rheology and Dynamics*, CRC Press.

Coussot, P. (2014), Yield stress fluid flows: A review of experimental data, *Journal of Non-Newtonian Fluid Mechanics*, *211*, 31–49, doi:10.1016/j.jnnfm.2014.05.006.

Coussot, P., and S. Proust (1996), Slow, unconfined spreading of a mudflow, *Journal of Geophysical Research: Solid Earth*, *101*(B11), 25217–25229, doi:10.1029/96JB02486.

Coussot, P., D. Laigle, M. Arattano, A. Deganutti, and L. Marchi (1998), Direct Determination of Rheological Characteristics of Debris Flow, *Journal of Hydraulic Engineering*, *124*(8), 865–868, doi:10.1061/(ASCE)0733-9429(1998)124:8(865).

de Haas, T., L. Braat, J. R. F. W. Leuven, I. R. Lokhorst, and M. G. Kleinhans (2015), Effects of debris flow composition on runout, depositional mechanisms, and deposit morphology in laboratory experiments: Experimental Debris Flows, *Journal of Geophysical*

Research: Earth Surface, *120*(9), 1949–1972, doi:10.1002/2015JF003525.

Delannay, R., A. Valance, A. Mangeney, O. Roche, and P. Richard (2017), Granular and particle-laden flows: from laboratory experiments to field observations, *Journal of Physics D: Applied Physics*, *50*(5), 053001, doi:10.1088/1361-6463/50/5/053001.

Domnik, B., and S. P. Pudasaini (2012), Full two-dimensional rapid chute flows of simple viscoplastic granular materials with a pressure-dependent dynamic slip-velocity and their numerical simulations, *Journal of Non-Newtonian Fluid Mechanics*, *173-174*, 72–86, doi:10.1016/j.jnnfm.2012.03.001.

Forterre, Y., and O. Pouliquen (2008), Flows of Dense Granular Media, *Annual Review of Fluid Mechanics*, *40*(1), 1–24, doi:10.1146/annurev.fluid.40.111406.102142.

Frigaard, I. A., and C. Nouar (2005), On the usage of viscosity regularisation methods for visco-plastic fluid flow computation, *Journal of Non-Newtonian Fluid Mechanics*, *127*(1), 1–26, doi:10.1016/j.jnnfm.2005.01.003.

Griffiths, R. W. (2000), The Dynamics of Lava Flows, *Annual Review of Fluid Mechanics*, *32*(1), 477–518, doi:10.1146/annurev.fluid.32.1.477.

Huang, X., and M. H. Garcia (1997), A Perturbation Solution for Bingham-Plastic Mudflows, *Journal of Hydraulic Engineering*, *123*(11), 986–994, doi:10.1061/(ASCE)0733-9429(1997)123:11(986).

Huang, X., and M. H. Garcia (1998), A Herschel–Bulkley model for mud flow down a slope, *Journal of Fluid Mechanics*, *374*, 305–333, doi:10.1017/S0022112098002845.

Hungr, O., S. Leroueil, and L. Picarelli (2014), The Varnes classification of landslide types, an update, *Landslides*, *11*(2), 167–194, doi:10.1007/s10346-013-0436-y.

Hürlimann, M., B. W. McArdell, and C. Rickli (2015), Field and laboratory analysis of the runout characteristics of hillslope debris flows in Switzerland, *Geomorphology*, *232*, 20–32, doi:10.1016/j.geomorph.2014.11.030.

Issler, D., F. De Blasio, A. Elverhøi, P. Bryn, and R. Lien (2005), Scaling behaviour of clay-rich submarine debris flows, *Marine and Petroleum Geology*, *22*(1-2), 187–194, doi:10.1016/j.marpetgeo.2004.10.015.

Iverson, R. M. (1997), The physics of debris flows, *Reviews of Geophysics*, *35*(3), 245–296, doi:10.1029/97RG00426.

Iverson, R. M. (2005), Debris-flow mechanics, in *Debris-flow Hazards and Related Phenomena*, Springer, Berlin Heidelberg.

Iverson, R. M. (2015), Scaling and design of landslide and debris-flow experiments, *Geomorphology*, *244*, 9–20, doi:10.1016/j.geomorph.2015.02.033.

Iverson, R. M., M. Logan, R. G. LaHusen, and M. Berti (2010), The perfect debris flow? Aggregated results from 28 large-scale experiments, *Journal of Geophysical Research*, *115*(F3), F03005, doi:10.1029/2009JF001514.

Jeong, S. W. (2013), Determining the viscosity and yield surface of marine sediments using modified Bingham models, *Geosciences Journal*, *17*(3), 241–247, doi:10.1007/s12303-013-0038-7.

Jeong, S. W., S. Leroueil, and J. Locat (2009), Applicability of power law for describing the rheology of soils of different origins and characteristics, *Canadian Geotechnical Journal*, *46*(9), 1011–1023, doi:10.1139/T09-031.

Jing, L., C. Y. Kwok, Y. F. Leung, and Y. D. Sobral (2016), Extended CFD-DEM for free-surface flow with multi-size granules, *International Journal for Numerical and Analytical*

Methods in Geomechanics, *40*(1), 62–79, doi:10.1002/nag.2387.

Johnson, C. G., B. P. Kokelaar, R. M. Iverson, M. Logan, R. G. LaHusen, and J. M. N. T. Gray (2012), Grain-size segregation and levee formation in geophysical mass flows, *Journal of Geophysical Research*, *117*(F1), F01032, doi:10.1029/2011JF002185.

Jop, P., Y. Forterre, and O. Pouliquen (2006), A constitutive law for dense granular flows, *Nature*, *441*(7094), 727–730, doi:10.1038/nature04801.

Kaitna, R., D. Rickenmann, and M. Schatzmann (2007), Experimental study on rheologic behaviour of debris flow material, *Acta Geotechnica*, *2*(2), 71–85, doi:10.1007/s11440-007-0026-z.

Kaitna, R., M. C. Palucis, B. Yohannes, K. M. Hill, and W. E. Dietrich (2016), Effects of coarse grain size distribution and fine particle content on pore fluid pressure and shear behavior in experimental debris flows, *Journal of Geophysical Research: Earth Surface*, *121*(2), 415–441, doi:10.1002/2015JF003725.

Kern, M., F. Tiefenbacher, and J. McElwaine (2004), The rheology of snow in large chute flows, *Cold Regions Science and Technology*, *39*(2-3), 181–192, doi: 10.1016/j.coldregions.2004.03.006.

Lacaze, L., and R. R. Kerswell (2009), Axisymmetric Granular Collapse: A Transient 3d Flow Test of Viscoplasticity, *Physical Review Letters*, *102*(10), doi: 10.1103/PhysRevLett.102.108305.

Lagrée, P.-Y., L. Staron, and S. Popinet (2011), The granular column collapse as a continuum: validity of a two-dimensional Navier–Stokes model with a μ(I)-rheology, *Journal of Fluid Mechanics*, *686*, 378–408, doi:10.1017/jfm.2011.335.

Legros, F. (2002), The mobility of long-runout landslides, *Engineering Geology*, *63*(3), 301–331, doi:The mobility of long-runout landslides.

Leonardi, A., M. Cabrera, F. K. Wittel, R. Kaitna, M. Mendoza, W. Wu, and H. J. Herrmann (2015), Granular-front formation in free-surface flow of concentrated suspensions, *Physical Review E*, *92*(5), 052204, doi:10.1103/PhysRevE.92.052204.

Leonardi, A., F. K. Wittel, M. Mendoza, R. Vetter, and H. J. Herrmann (2016), Particle–Fluid–Structure Interaction for Debris Flow Impact on Flexible Barriers, *Computer-Aided Civil and Infrastructure Engineering*, *31*, 323–333, doi:10.1111/mice.12165.

Liu, Y., N. Balmforth, S. Hormozi, and D. Hewitt (2016), Two–dimensional viscoplastic dambreaks, *Journal of Non-Newtonian Fluid Mechanics*, *238*, 65–79, doi:10.1016/j.jnnfm.2016.05.008.

Lucas, A., A. Mangeney, and J. P. Ampuero (2014), Frictional velocity-weakening in landslides on Earth and on other planetary bodies, *Nature Communications*, *5*, 3417, doi:10.1038/ncomms4417.

Malin, M. R. (1997), The turbulent flow of Bingham plastic fluids in smooth circular tubes, *International Communications in Heat and Mass Transfer*, *24*(6), 793–804.

Martin, N., I. R. Ionescu, A. Mangeney, F. Bouchut, and M. Farin (2017), Continuum viscoplastic simulation of a granular column collapse on large slopes: μ(I) rheology and lateral wall effects, *Physics of Fluids*, *29*(1), 013301, doi:10.1063/1.4971320.

Martinez, C. E. (2009), Eulerian-Lagrangian Two Phase Debris Flow Model, Ph.D. thesis, Florida International University, USA.

Mitsoulis, E. (2007), Flows of viscoplastic materials: models and computations, *Rheology Reviews*, 135–178.

O'Donovan, E. J., and R. I. Tanner (1984), Numerical study of the Bingham squeeze film problem, *Journal of Non-Newtonian Fluid Mechanics*, *15*(1), 75–83, doi:10.1016/0377-0257(84)80029-4.

OpenCFD (2016), OpenFOAM® - The Open Source Computational Fluid Dynamics (CFD) Toolbox.

Papanastasiou, T. C., and A. G. Boudouvis (1997), Flows of viscoplastic materials: Models and computations, *Computers & Structures*, *64*(1), 677–694, doi:10.1016/S0045-7949(96)00167-8.

Parez, S., and E. Aharonov (2015), Long runout landslides: a solution from granular mechanics, *Frontiers in Physics*, *3*, doi:10.3389/fphy.2015.00080.

Parsons, J. D., K. X. Whipple, and A. Simoni (2001), Experimental study of the grain-flow, fluid-mud transition in debris flows, *The Journal of Geology*, *109*(4), 427–447.

Pudasaini, S. P. (2012), A general two-phase debris flow model, *Journal of Geophysical Research: Earth Surface*, *117*(F3), F03010, doi:10.1029/2011JF002186.

Rickenmann, D. (2005), Runout prediction methods, in *Debris-flow Hazards and Related Phenomena*, Springer, Berlin Heidelberg.

Roche, O., M. Attali, A. Mangeney, and A. Lucas (2011), On the run-out distance of geophysical gravitational flows: Insight from fluidized granular collapse experiments, *Earth and Planetary Science Letters*, *311*(3-4), 375–385, doi:10.1016/j.epsl.2011.09.023.

Rusche, H. (2002), Computational fluid dynamics of dispersed two-phase flows at high phase fractions, Ph.D. thesis, Imperial College, UK.

Sakimoto, S. E. H., and T. K. P. Gregg (2001), Channeled flow: Analytic solutions, laboratory experiments, and applications to lava flows, *Journal of Geophysical Research:*

Solid Earth, *106*(B5), 8629–8644, doi:10.1029/2000JB900384.

Savage, S. B., and K. Hutter (1989), The motion of a finite mass of granular material down a rough incline, *Journal of Fluid Mechanics*, *199*, 177–215, doi: 10.1017/S0022112089000340.

Scardovelli, R., and S. Zaleski (1999), Direct numerical simulation of free-surface and interfacial flow, *Annual review of fluid mechanics*, *31*(1), 567–603.

Sham, C. M. (2015), Landslide mobility factors at Tsing Shan area, *HKU Theses Online (HKUTO)*.

Staron, L. (2008), Mobility of long-runout rock flows: a discrete numerical investigation, *Geophysical Journal International*, *172*(1), 455–463, doi:10.1111/j.1365-246X.2007.03631.x.

Staron, L., and E. J. Hinch (2007), The spreading of a granular mass: role of grain properties and initial conditions, *Granular Matter*, *9*(3-4), 205–217, doi:10.1007/s10035-006-0033-z.

Staron, L., and E. Lajeunesse (2009), Understanding how volume affects the mobility of dry debris flows, *Geophysical Research Letters*, *36*(12), doi:10.1029/2009GL038229.

Staron, L., P.-Y. Lagrée, P. Ray, and S. Popinet (2013), Scaling laws for the slumping of a Bingham plastic fluid, *Journal of Rheology*, *57*(4), 1265, doi:10.1122/1.4802052.

Takahashi, T. (1981), Debris flow, *Annual review of fluid mechanics*, *13*(1), 57–77.

von Boetticher, A., J. M. Turowski, B. W. McArdell, D. Rickenmann, and J. W. Kirchner (2016), DebrisInterMixing-2.3: a finite volume solver for three-dimensional debris-flow simulations with two calibration parameters – Part 1: Model description, *Geoscientific Model Development*, *9*(9), 2909–2923, doi:10.5194/gmd-9-2909-2016.

Zakeri, A., K. Høeg, and F. Nadim (2008), Submarine debris flow impact on pipelines — Part I: Experimental investigation, *Coastal Engineering*, *55*(12), 1209–1218, doi: 10.1016/j.coastaleng.2008.06.003.

Zakeri, A., K. Høeg, and F. Nadim (2009), Submarine debris flow impact on pipelines — Part II: Numerical analysis, *Coastal Engineering*, *56*(1), 1–10, doi: 10.1016/j.coastaleng.2008.06.005.

Table 1. Rheological parameters of slurries.

			Bingham		Herschel–Bulkley		
Slurry	C_v (%)	ρ (kg/m^3)	τ_y (Pa)	μ_B (Pa $\cdot$ s)	τ_c (Pa)	K (Pa $\cdot$ s^n)	n
1	17	1298	12.32	0.0065	9.71	0.17	0.59
2	18	1324	18.80	0.0081	12.94	1.14	0.36
3	19	1332	23.95	0.011	15.18	2.15	0.31
4	20	1354	30.36	0.012	17.56	3.66	0.27
5	21.1	1368	39.09	0.017	21.26	5.68	0.25

Table 2. Deposit runout length (L_r) and maximum width (W_m) for each experiment

Series	C_v(%)	θ(°)	V (L)	L_r(m)	W_m(m)
Reference cases	18	14	3.06	0.95	0.39
	19	14	3.06	0.67	0.35
	20	14	3.09	0.55	0.33
	21.1	14	3.00	0.27	0.32
Different volumes	19	14	2.00	0.43	0.29
	19	14	4.00	0.91	0.42
	20	14	2.17	0.33	0.29
	20	14	3.07	0.57	0.33
	21.1	14	2.17	0.13	0.26
	21.1	14	3.72	0.42	0.34
	21.1	14	3.99	0.45	0.35
	21.1	14	4.34	0.54	0.40
Different slope angles	19	16	2.98	0.78	0.35
	20	16	3.01	0.60	0.34
	21.1	16	3.00	0.50	0.34

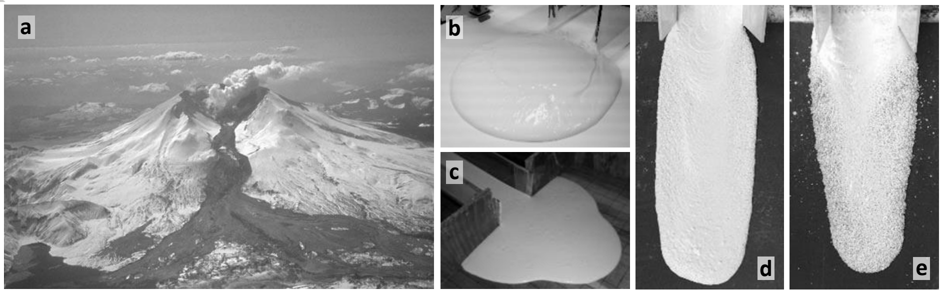

Figure 1. Mudflow deposits. (a) Lahar (dark deposit on snow) on Mount St. Helens after the March 19, 1982, eruption (Photograph by Tom Casadevall, U.S. Geological Survey). (b) Semi-circular deposit of a Carpobol solution (Photography by Environmental Hydraulics Laboratory, EPFL) [*Cochard and Ancey*, 2009]. (c) Hill-shape deposit of a kaolin slurry [*Martinez*, 2009]. (d) Elongated deposit of a mixture of water and fine particles (Photograph by Dingchen Zhang, The University of Hong Kong). (e) Elongated deposit of a mixture of water, fine and coarse particles (Photograph by Dingchen Zhang, The University of Hong Kong).

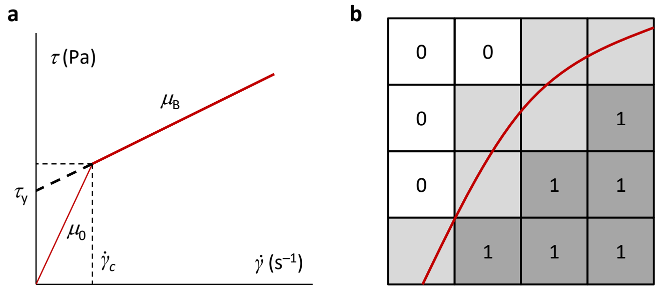

Figure 2. Key numerical schemes. (a) Bi-viscosity regularization of Bingham model. (b) Volume of fluid (VOF) method.

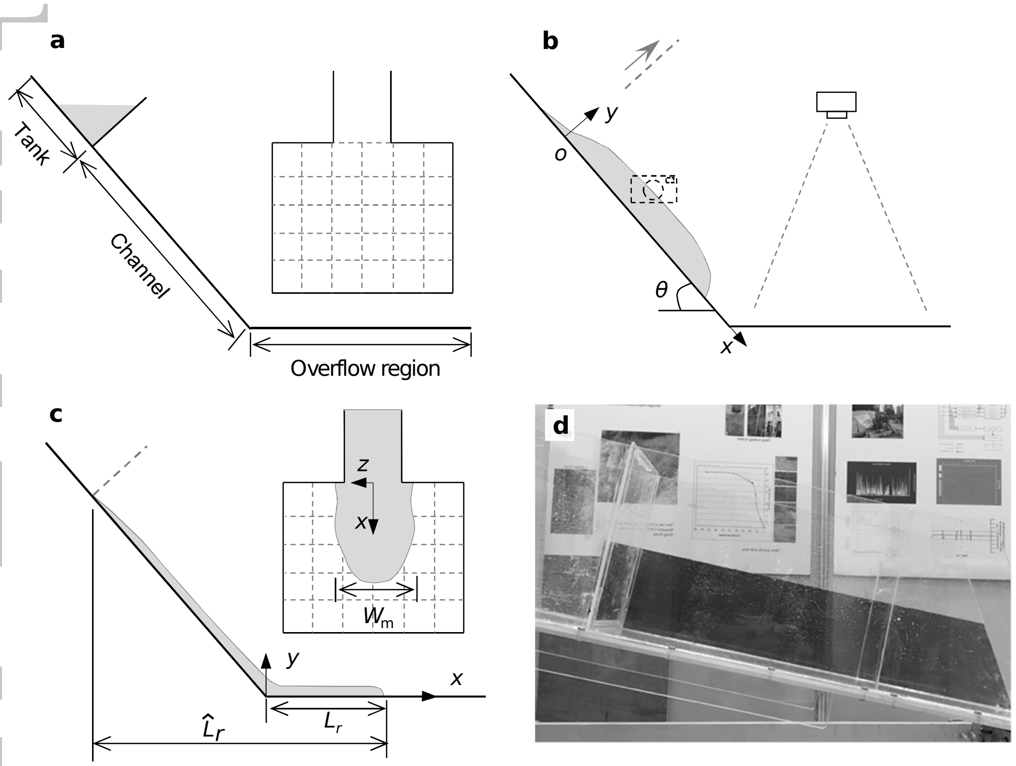

Figure 3. Flume setup. (a) Initial configuration in side- and plan-views. (b) Flow measurements by cameras looking through the sidewall of the flume and downward over the deposition plain. Local coordinates down channel: x and y are, respectively, the longitudinal and vertical directions along the inclined channel. (c) Final configuration, runout distance and deposit profile. Local coordinates at runout: x, y, and z are, respectively, the longitudinal, vertical, and lateral directions on the deposition plain, with an origin at the toe of the slope, where the mudflow exits the channel. (d) Side-view photo of the flume.

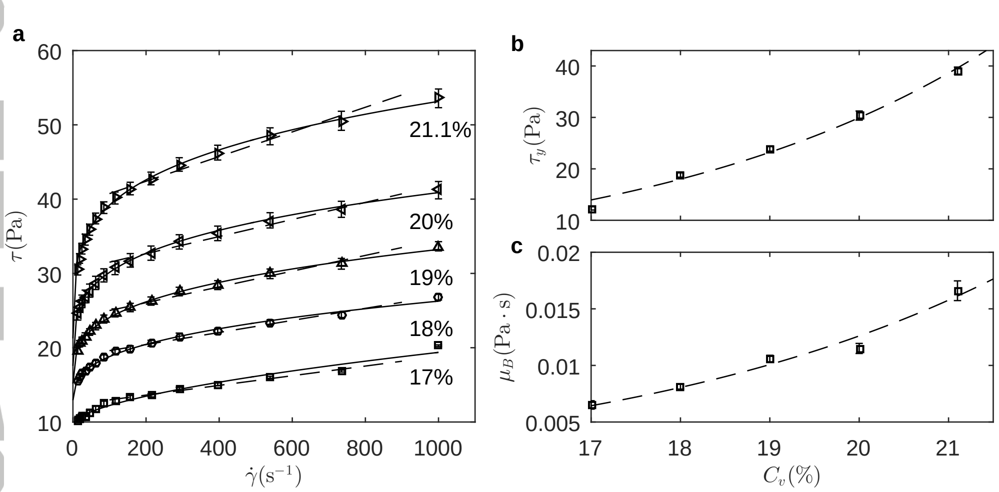

Figure 4. Rheology measurements. (a) Flow curves expressed as shear rate and applied shear stress for different volume concentrations. Symbols are measured data, solid lines are fitted by the Herschel–Bulkley model, while dashed lines are fitted by the Bingham model (see Table 1). (b) Yield stress as a function of concentration. (c) Viscosity as a function of concentration.

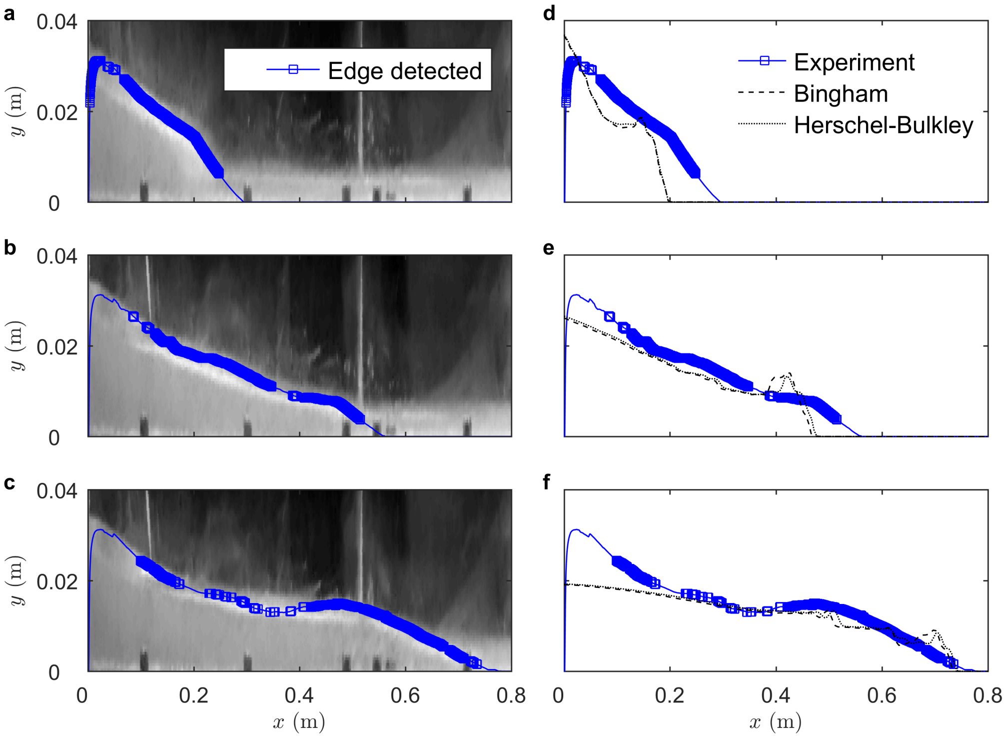

Figure 5. Validation of side-view flow profiles on the channel ($V = 3$ L, $\theta = 14^\circ$, $C_v = 20\%$). The coordinate system is shown in Figure 3b. (a–c) Experiment frames and the detection of flow-depth profiles, for $t \approx 0.2, 0.4, 0.6$ s, respectively. (d–e) Comparison of flow-depth profiles between experiments and simulations, using Bingham and Herschel–Bulkley models, for $t \approx 0.2, 0.4, 0.6$ s, respectively.

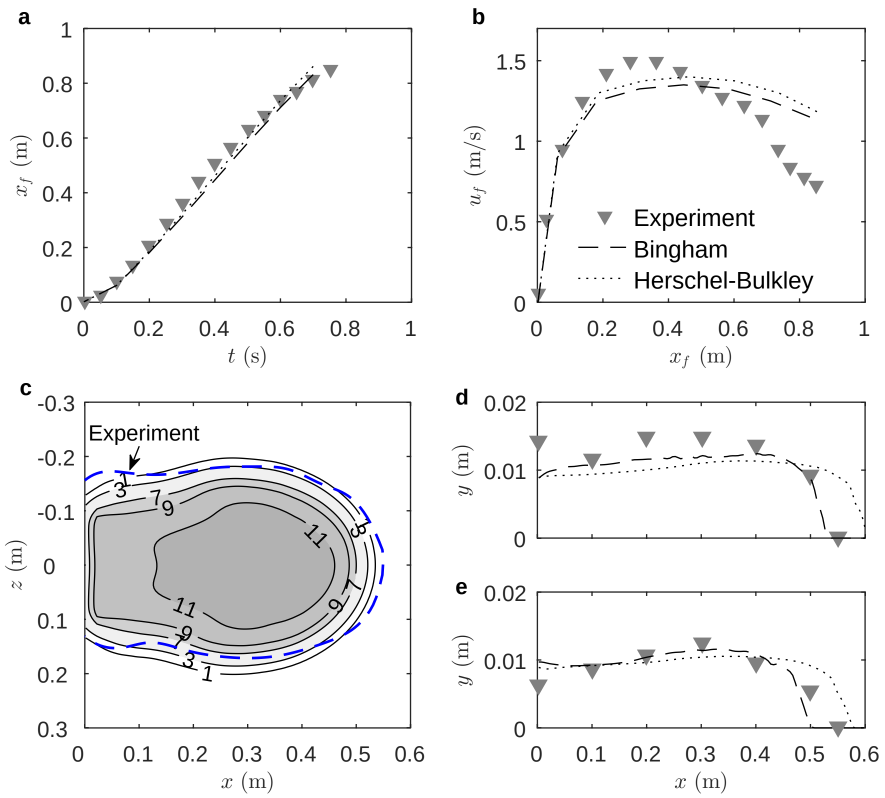

Figure 6. Validation of front propagation and final deposition ($V = 3$ L, $\theta = 14°$, $C_v = 20\%$). The coordinate systems of the upper and lower panels are shown in Figure 3b and Figure 3c, respectively. (a) Front position as a function of time. (b) Frontal velocity at different travel distances. (c) Contour plot of final deposits. Contour labels are depth in mm. Results from the Herschel–Bulkley model are omitted in (c) for clarity. (d) Deposit depth at $z = 0.1$ m. (e) Deposit depth at centerline ($z = 0$).

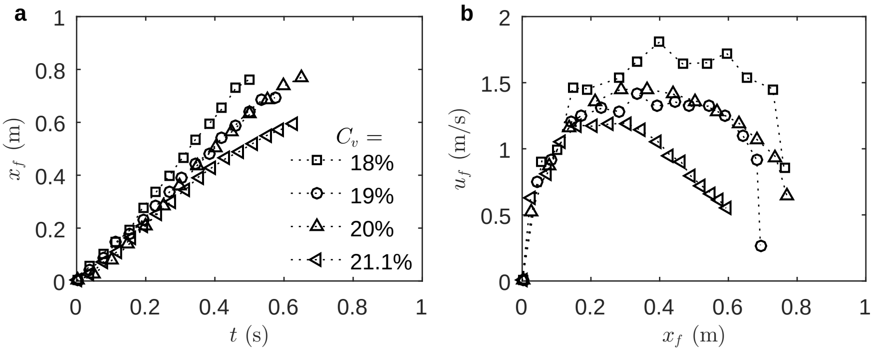

Figure 7. Experimental results on the channel ($V = 3$ L, $\theta = 14°$, $C_v = 18\%, 19\%, 20\%, 21.1\%$).

(a) Front position as a function of time. (b) Frontal velocity at different travel distance.

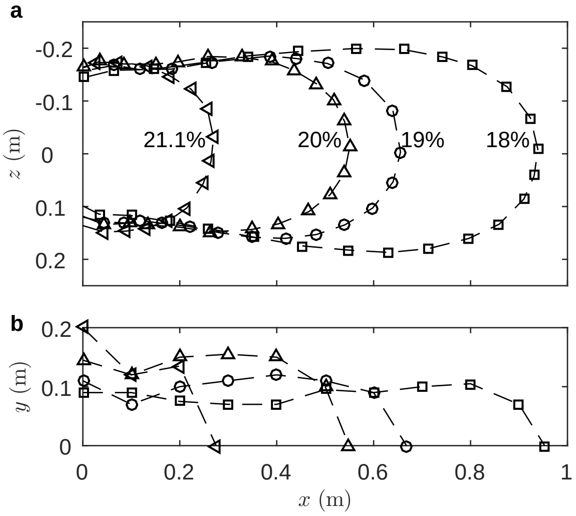

Figure 8. Experimental results at the deposition region. (a) Deposit shapes for different concentrations. (b) Depth profiles at the centerline for different concentrations.

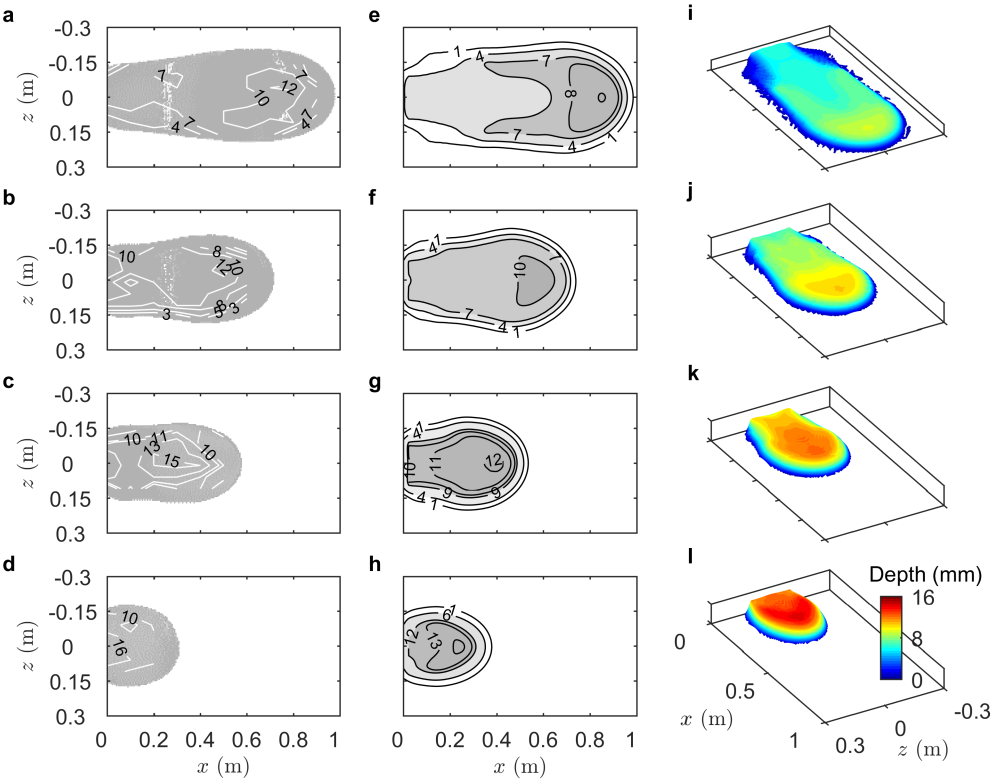

Figure 9. Deposit morphology of the four experiments ($C_v = 18\%, 19\%, 20\%, 21.1\%$, respectively, from top to bottom). (a–d) Experimental photos with contours of measured deposit depth. The different shading of pixels is due to the reflection of light when photos are taken. Contour labels are deposit depth in mm. (e–h) Contour plots from simulations. (i–l) Three-dimensional mesh plots from simulations. The axis in the y-direction is exaggerated by 5 times.

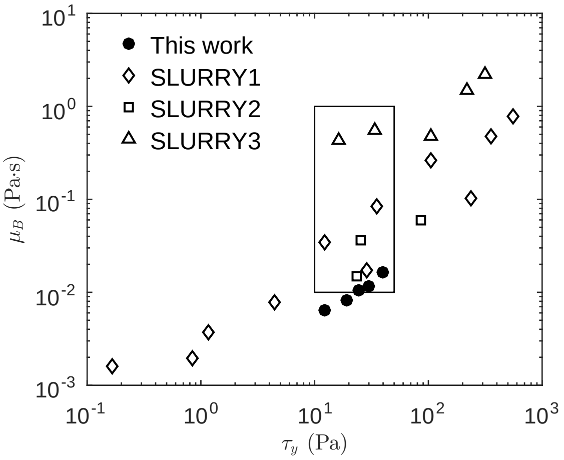

Figure 10. Parameter space for simulations (inside the rectangle) and the correlation between μ_B and τ_y for slurries. SLURRY1 and SLURRY2 represent the kaolin–water slurries tested in *Coussot* [1997] and *Martinez* [2009], respectively. SLURRY3 is the slurry made from debris flow materials [*Kaitna et al.*, 2007]. The slurry used in this work is also presented (the filled circles).

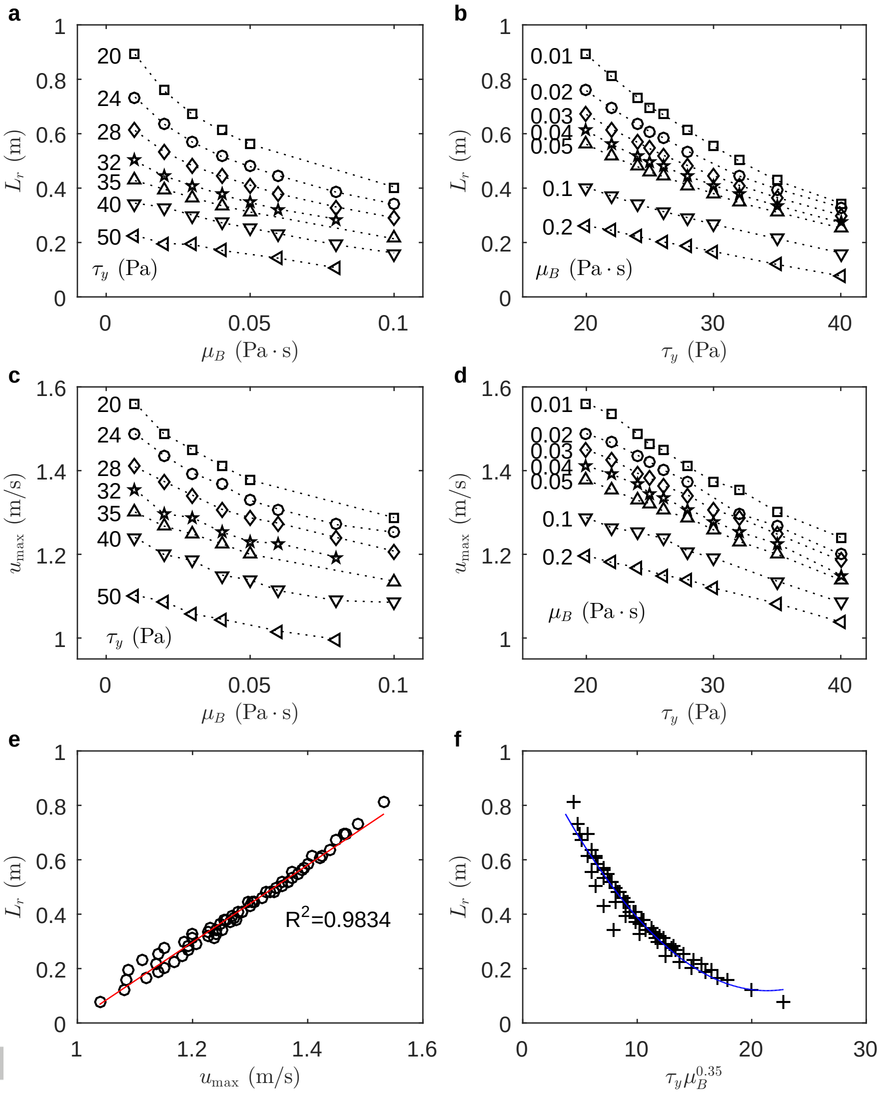

Figure 11. Simulation results with different combinations of μ_B and τ_y. (a,b) Separate effects of μ_B and τ_y on L_r. (c,d) Separate effects of μ_B and τ_y on $u_{\max}$. (e) Correlation between $u_{\max}$ and L_r. (f) L_r as a function of the combination $\tau_y \mu_B^{0.35}$.

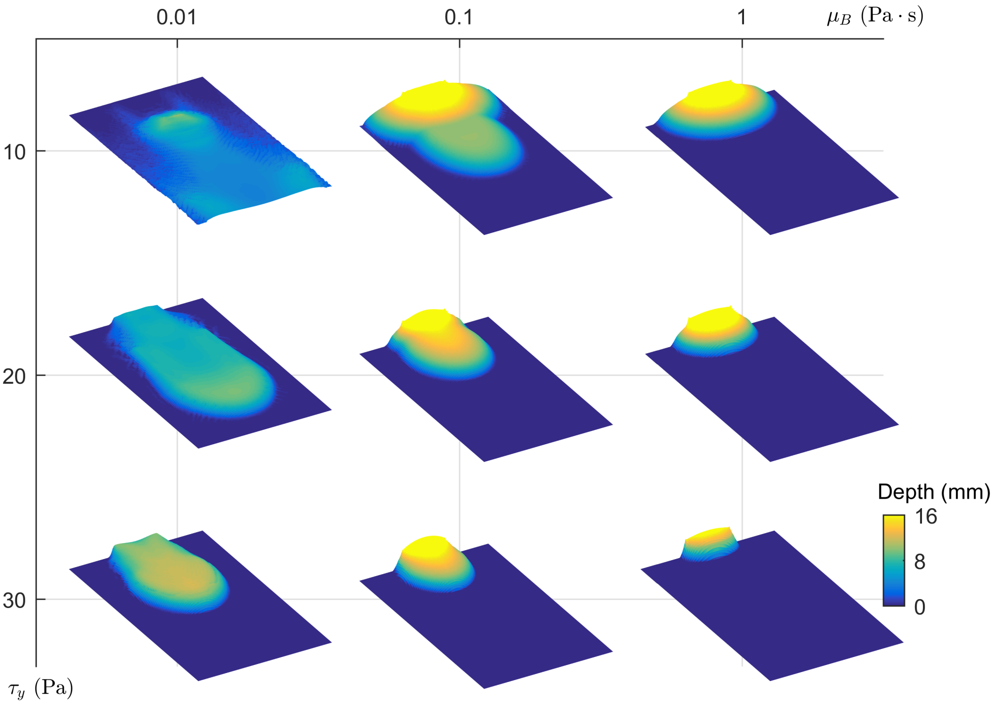

Figure 12. Predicted deposit morphology for different combinations of μ_B and τ_y. The vertical axis of each contour plot is exaggerated by 5 times.

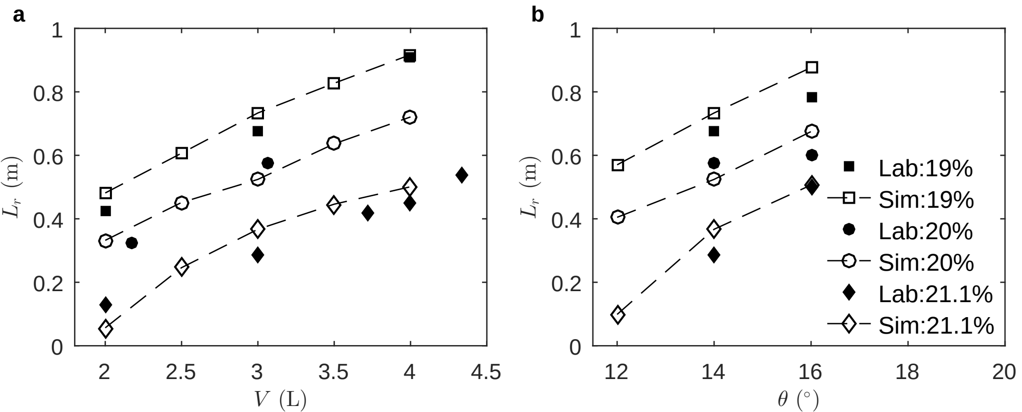

Figure 13. Effects of V and θ on L_r in both experiments and simulations. (a) Varying V with $\theta = 14°$. (b) Varying θ with $V = 3$ L.

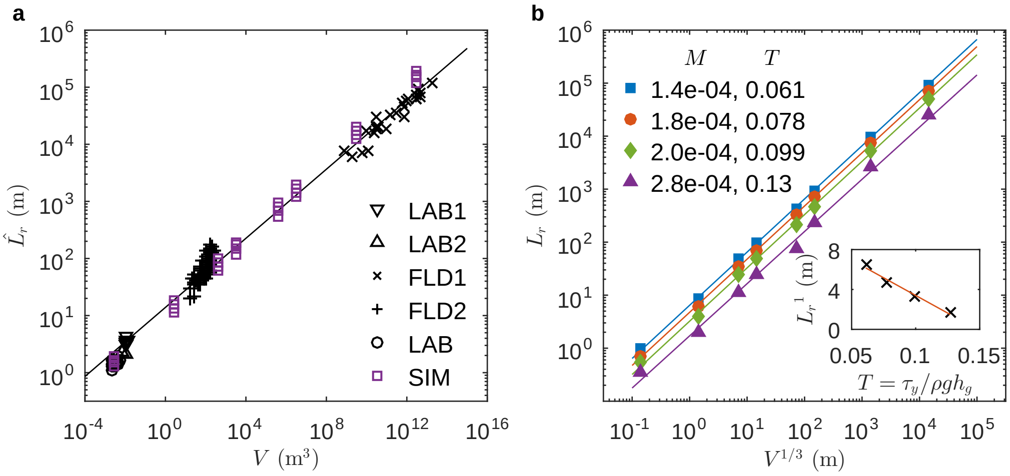

Figure 14. Runout scaling. (a) Comparison with literature data. Legend items LAB1 and LAB2 represent laboratory data from *Chan* [2001] and *Martinez* [2009], respectively; FLD1 and FLD2 represent field data reported in *Legros* [2002] and *Sham* [2015], respectively. LAB refers to all laboratory experiments done in our current study, while SIM denotes our numerical simulations. (b) Correlation between L_r and V for different combinations of M and T. The two numbers in each legend item are the values of M and T, respectively. Inset: L_r^1 as a function of T, where L_r^1 is the fitted value of L_r at $V^{1/3} = 1$ m.

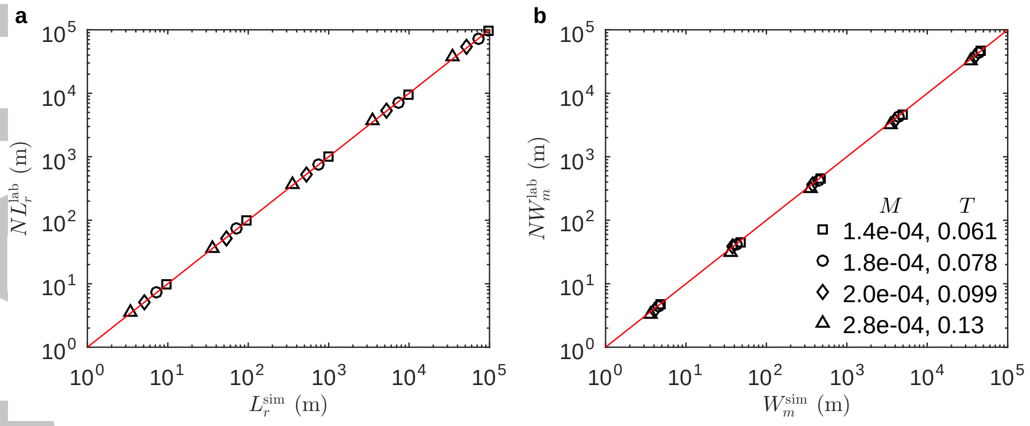

Figure 15. Verification of the scaling rules (equation (7)) for $N = 10, 100, 1000, 10000, 100000$. The two numbers in each legend item are the values of M and T, respectively. (a) Runout distance from simulations at different scales, $L_r^{\rm sim}$, compared with the theoretical values, $NL_r^{\rm lab}$. (b) The maximum deposit width from simulations at different scales, $W_m^{\rm sim}$, compared with the theoretical values, $NW_m^{\rm lab}$.